JOURNAL OF AIRCRAFT
Vol. 38, No. 5, September–October 2001

Effect of Wake Adaptation on Rotor Hover Simulations Using Unstructured Meshes

Hee Jung Kang* and Oh Joon Kwon†
Korea Advanced Institute of Science and Technology, Taejon 305-701, Republic of Korea

A three-dimensional inviscid flow solver is developed for simulating the flowfield of hovering helicopter rotor using unstructured meshes. The flow solver utilizes a cell-centered finite volume scheme that is based on the Roe's flux-difference splitting with an implicit Jacobi/Gauss–Seidel time integration. Calculations are performed at two operating conditions of subsonic and transonic tip Mach numbers. A solution-adaptive mesh refinement technique is adopted to improve the resolution of flow features on the blade surface. It is demonstrated that the trajectory of the tip vortex can be captured through a series of adaptive mesh refinements starting from a very coarse initial grid. It was found that not only the strength of the tip vortex, but also its trajectory, is strongly dependent on the mesh resolution in the wake. Good agreement is obtained between the numerical result and the experiment for both the blade loading and the tip vortex behavior.

Nomenclature

a_∞	=	freestream speed of sound
C_p	=	rotor sectional pressure coefficient, $(p - p_\infty)/[0.5\rho_\infty(\Omega r)^2]$
C_T	=	rotor thrust coefficient, $T/[\pi\rho_\infty R^2(\Omega R)^2]$
C_t	=	rotor blade sectional thrust coefficient, $(\mathrm{d}T/\mathrm{d}r)/[0.5c\rho_\infty(\Omega R)^2]$
c	=	rotor blade chord
e_0	=	total energy per unit volume
M_T	=	rotor tip Mach number, $(\Omega R)/a_\infty$
p	=	fluid pressure
p_∞	=	freestream pressure
R	=	rotor radius
r	=	radial distance along blade span
r_c	=	radius of tip vortex core
T	=	rotor thrust
U	=	inertial velocity component normal to control volume surface
U_r	=	relative velocity component normal to control volume surface
u, v, w	=	Cartesian velocity components in inertial frame
x, y, z	=	Cartesian coordinates in inertial frame
Γ	=	circulation of tip vortex
ρ	=	fluid density
ρ_∞	=	freestream density
Ψ	=	vortex age of tip vortex
Ω	=	rotor angular velocity in the z direction
ω	=	local vorticity inside tip vortex core

Superscript

$\sim$	=	Roe-averaged quantity

Introduction

ACCURATE numerical simulation of the flowfield of helicopter rotors is one of the most complicated and challenging problems in the field of aerodynamics. To predict the performance of helicopter rotors, the numerical method must have a capability of accurately capturing the flow not only on the blade but also in the vortical wake generated from the rotor blade tip, which significantly affects the overall performance, vibration, and noise. Traditionally, the wake effect has been approximated using models such as prescribed or free wakes coupled with the lifting-line, lifting-surface, full-potential, and Euler/Navier–Stokes methods.[1–6] Recently, direct wake capturing methods based on the structured grid have been suggested.[7–10] The computational grid covers the entire flowfield of helicopter rotor and its wake so that no wake model is required. Even though structured grid methods avoid the problem of modeling the complicated wake, which is strongly dependent on the rotor geometry and the operating condition, these methods still have an inherent deficiency in predicting the rotor performance accurately. The tip-vortex capturing requires very fine meshes, where the tip vortex is located to avoid the numerical dissipation inherent in computational fluid dynamics (CFD) methods, which results in wasting many grid points in the computational domain away from the tip vortex and the rotor blade due to the nature of the structured grid. Proper mesh arrangement for the tip vortex is a very difficult task because its trajectory is usually not known in advance. Some researchers utilize the overset-grid topology for the calculation of rotor performance and wake capturing. Hariharan and Sankar[11] suggested a seventh-order spatially accurate scheme and a moving overset grid to capture accurately the rotor and wing tip vortices. Tang and Baeder[12] used a grid redistribution methodology to reduce the numerical dissipation of vorticity and compared the predicted tip vortex core growth with the experimental data. Ahmad and Strawn[13] used an overset-grid viscous method and investigated the dependency of three different wake grid resolutions. They successfully tracked the tip vortex for 630 deg of vortex age using up to 17.1×10^6 grid points at the finest level.

In contrast, the unstructured mesh methodology utilizes randomly distributed mesh cells so that addition and deletion of grid points on existing meshes are naturally easy as long as the cell connectivity is properly taken care of. Thus, the unstructured mesh technique enables a user to refine the mesh as much as needed at the local flow region of interest. Thus, the technique based on the unstructured mesh CFD greatly relieves the difficulty structured grids have when applied to helicopter rotor aerodynamic problems. Whereas the tip vortex strength can be well preserved by providing a sufficient number of cells through the solution-adaptive grid refinement along the tip vortex trajectory, the grid density at the far field away from the blade can be kept low to minimize the computer resource requirements. The solution is obtained through several steps of adaptive mesh refinement as the calculation evolves by searching for cells with concentrated vorticity. Thus, the tip vortex geometry can be naturally captured, while providing accurate influences on the blades.

Presented as Paper 2000-0258 at the AIAA 38th Aerospace Sciences Meeting and Exhibit, Reno, NV, 10–13 January 2000; received 17 May 2000; revision received 8 May 2001; accepted for publication 5 June 2001.

*Doctoral Candidate, Department of Aerospace Engineering, 373-1 Kusong-Dong, Yusong-Gu.

†Associate Professor, Department of Aerospace Engineering, 373-1 Kusong-Dong, Yusong-Gu. Senior Member AIAA.

Several attempts have been made to predict the performance of hovering rotors using unstructured adaptive meshes. The first unstructured mesh methodology applied to rotor flow computations was carried out by Strawn and Barth[14] using an explicit time integration and a finite volume scheme. The unstructured mesh was obtained by dividing regular structured grids into tetrahedron. The mesh was refined along the trace of the tip vortex, which was experimentally predetermined. The tip vortex structure was captured successfully up to 270 deg of vortex age using more than 1.4×10^6 tetrahedra at the finest adaptation level. Duque et al.[15] used overset structured/unstructured grids with a thin-layer Navier–Stokes flow solver. Various adaptation indicators were implemented to distribute the grid points properly for the solution-adaptive mesh refinement. Dindar et al.[16] recently used a finite element method on unstructured meshes to locate the vortex core trajectory by introducing a critical theory based on the eigenvalues of the velocity-gradient tensor for mesh refinement. After the third-level mesh refinement, the total number of elements reached 2.3×10^6 starting from an initial mesh of 1.2×10^6.

Even though these unstructured mesh calculations were very successful in accurately predicting the aerodynamic performance and capturing the tip vortex trajectory through sequential refinements of the mesh along the tip vortex, a certain degree of initial mesh resolution was required to initiate the tip vortex capturing so that the tip vortex evolves without too much numerical dissipation. This eliminates much of the advantage of using the unstructured meshes for rotor aerodynamic problems. In the present study, an attempt is made to demonstrate numerically the capability of tracing the hovering rotor tip vortex trajectory through a series of spatial mesh adaptations starting from a very coarse initial grid. The effect of mesh refinement on the flowfield of the rotor and the tip vortex is studied. For the present purpose, a three- dimensional inviscid unstructured mesh parallel flow solver is developed based on a cell-centered finite volume scheme with the Roe's flux-difference splitting. An implicit Jacobi/Gauss–Seidel method is used for time integration. Calculations are validated by comparing the results with available experimental data.[17]

Numerical Method

Governing Equations

The equations governing three-dimensional, inviscid, unsteady, compressible flows are the Euler equations, which express the conservation of mass, momentum, and energy for a Newtonian fluid in the absence of external forces. The equations can be recast for helicopter rotors for absolute flow variables on a rotational frame of reference. The equations may be written in an integral form for a bounded domain V with a boundary ∂V:

$$\frac{\partial}{\partial t}\int_V \boldsymbol{Q}\,\mathrm{d}V + \oint_{\partial V} \boldsymbol{F}(\boldsymbol{Q},\boldsymbol{n})\,\mathrm{d}S = \int_V \boldsymbol{S}\,\mathrm{d}V \tag{1}$$

where

$$\boldsymbol{Q} = \begin{pmatrix} \rho \\ \rho u \\ \rho v \\ \rho w \\ e_0 \end{pmatrix}, \qquad \boldsymbol{F}(\boldsymbol{Q},\boldsymbol{n}) = \begin{pmatrix} \rho U_r \\ \rho u U_r + p n_x \\ \rho v U_r + p n_y \\ \rho w U_r + p n_z \\ e_0 U_r + p U \end{pmatrix}$$

$$\boldsymbol{S} = \begin{pmatrix} 0 \\ \Omega\rho v \\ -\Omega\rho u \\ 0 \\ 0 \end{pmatrix}$$

where Ω is the rotor angular velocity relative to the inertial frame and n_x, n_y, and n_z are the Cartesian components of the exterior surface unit normal $\boldsymbol{n}$ on the boundary ∂V. U_r is the normal relative velocity on the rotational frame. All variables are normalized by the freestream density, the freestream speed of sound, and the rotor chord length. Equation (1) describes a relationship where the time rate of change of the state vector $\boldsymbol{Q}$ within the domain V is balanced by the net flux $\boldsymbol{F}$ across the boundary surface ∂V. The domain is divided into a finite number of tetrahedral cells, and Eq. (1) is applied to each cell. The state variables $\boldsymbol{Q}$ are volume-averaged values.

Spatial Discretization

The inviscid flux across each cell face κ is computed using Roe's flux-difference splitting formula[18]:

$$\boldsymbol{F}_\kappa = \tfrac{1}{2}[\boldsymbol{F}(\boldsymbol{Q}_L) + \boldsymbol{F}(\boldsymbol{Q}_R) - |\tilde{\boldsymbol{A}}|(\boldsymbol{Q}_R - \boldsymbol{Q}_L)]_\kappa \tag{2}$$

where $\boldsymbol{Q}_L$ and $\boldsymbol{Q}_R$ are the state variables to the left and right of the interface κ and $\tilde{\boldsymbol{A}}$ is the Jacobian matrix of Roe-averaged flow quantities. The last term in Eq. (2) can be represented as

$$|\tilde{\boldsymbol{A}}|(\boldsymbol{Q}_R - \boldsymbol{Q}_L) = \begin{pmatrix} \alpha_4 \\ \tilde{u}\alpha_4 + n_x\alpha_5 + \alpha_6 \\ \tilde{v}\alpha_4 + n_y\alpha_5 + \alpha_7 \\ \tilde{w}\alpha_4 + n_z\alpha_5 + \alpha_8 \\ \tilde{h}\alpha_4 + \tilde{U}\alpha_5 + \tilde{u}\alpha_6 + \tilde{v}\alpha_7 + \tilde{w}\alpha_8 - \dfrac{\tilde{a}^2}{\gamma - 1}\alpha_1 \end{pmatrix}$$

where h is the total enthalpy, a is the sound speed, and U is the normal velocity component of the fluid. The details of α can be found in Ref. 19.

For a first-order scheme, the state of the primitive variables at each cell face is set to the cell-centered average on either side of the face. For a higher-order scheme, estimation of the state at each cell face is achieved by interpolating the solution with a Taylor series expansion in the neighborhood of each cell center. The cell-averaged solution gradient required at the cell center for the preceding expansion is computed using Gauss's theorem by evaluating the surface integral for the closed surface of the tetrahedra. This process can be simplified using some geometrical invariant features of the tetrahedra.[20] The expansion also requires the nodal value of the solution, which can be computed from the surrounding cell center data using a second-order accurate pseudo-Laplacian averaging procedure as suggested by Holmes and Connell.[21]

Time Integration

A semidiscrete form of the governing equations can be written as

$$V_i \frac{\partial \boldsymbol{Q}_i}{\partial t} + \bar{\boldsymbol{R}}_i = 0, \qquad i = 1, 2, 3, \ldots \tag{3}$$

where V_i is the cell volume and $\bar{\boldsymbol{R}}_i$ is the residual accrued by summation of the inviscid fluxes and the source term through the four faces of a tetrahedral cell i.

The implicit scheme is obtained by evaluating the residual $\bar{\boldsymbol{R}}_i$ at the time level $n+1$ and by using the Euler backward difference for time:

$$V_i \frac{\Delta \boldsymbol{Q}_i}{\Delta t} + \bar{\boldsymbol{R}}_i^{n+1} = 0 \tag{4}$$

where $\Delta \boldsymbol{Q}_i = \boldsymbol{Q}_i^{n+1} - \boldsymbol{Q}_i^n$. The residual $\bar{\boldsymbol{R}}_i^{n+1}$ is linearized at the time level n as

$$\bar{\boldsymbol{R}}_i^{n+1} = \bar{\boldsymbol{R}}_i^n + \frac{\partial \bar{\boldsymbol{R}}_i^n}{\partial \boldsymbol{Q}} \Delta \boldsymbol{Q} \tag{5}$$

Here, $\partial \bar{\boldsymbol{R}}_i^n / \partial \boldsymbol{Q}$ is the Jacobian matrix that arises from the linearization process. The Jacobian is a very large sparse matrix because the stencil of the high-order flux discretization at each cell face is based on its nodes and the neighboring cell centers. To reduce the number of stencils involved and to enhance the diagonal dominance for numerical stability, only a first-order upwind approximation of the inviscid flux is used in the present implementation. To avoid

the complexity and to reduce the computational cost in linearizing Roe's flux-difference splitting scheme,[18] the Jacobian matrix of Roe-averaged flow quantities in Eq. (2) is frozen. This does not affect the high-order spatial accuracy of the present scheme to obtain steady-state solutions. The resulting implicit form of the governing equations for each tetrahedral cell i can be written as

$$\left[\frac{V_i}{\Delta t}\boldsymbol{I} + \sum_{j=1}^{4}\frac{\partial \boldsymbol{F}_{i,j}^n}{\partial \boldsymbol{Q}_i}S_{i,j} - V_i\frac{\partial \boldsymbol{S}_i^n}{\partial \boldsymbol{Q}_i}\right]\Delta \boldsymbol{Q}_i + \sum_{j=1}^{4}\frac{\partial \boldsymbol{F}_{i,j}^n}{\partial \boldsymbol{Q}_j}S_{i,j}\Delta \boldsymbol{Q}_j = -\sum_{j=1}^{4}\boldsymbol{F}_{i,j}^n S_{i,j} + V_i\boldsymbol{S}_i^n \tag{6}$$

where

$$\left.\frac{\partial \boldsymbol{F}_{i,j}}{\partial \boldsymbol{Q}_k}\right|_{k=i,j} = \frac{1}{2}\left[\frac{\partial \boldsymbol{F}(\boldsymbol{Q}_L)}{\partial \boldsymbol{Q}_L} + |\tilde{\boldsymbol{A}}|\right]\frac{\partial \boldsymbol{Q}_L}{\partial \boldsymbol{Q}_k} + \frac{1}{2}\left[\frac{\partial \boldsymbol{F}(\boldsymbol{Q}_R)}{\partial \boldsymbol{Q}_R} - |\tilde{\boldsymbol{A}}|\right]\frac{\partial \boldsymbol{Q}_R}{\partial \boldsymbol{Q}_k}$$

where subscript j represents the surrounding cell index of the current cell i.

A direct solution of the system of simultaneous equations resulting from the application of Eq. (6) for entire cells requires the inversion of a large spare matrix, which is computationally very expensive. Instead, a Gauss–Seidel relaxation approach is used to solve the equations iteratively so that the summation involving $\Delta \boldsymbol{Q}_j$ is moved to the right-hand side of Eq. (6). The summation at a given time step is evaluated using the most recent values of $\Delta \boldsymbol{Q}_j$. A cell-coloring scheme is implemented by regrouping cells so that no two cells in a given group share a common face. The cells belong to the first group are solved using a Jacobi-type iteration. The cells in the subsequent groups are solved using a Gauss–Seidel iteration. The details of coloring procedure can be found in Ref. 22. To accelerate the convergence of the solution to steady state, local time stepping is also used.

Boundary Condition

At the solid wall, the slip boundary condition is used for inviscid flows. The flow tangency condition is implemented by imposing no flux through the wall. The grid velocity due to the rotation is also accounted for at the solid surface. Density and pressure are extrapolated from the interior. The flux Jacobian at the wall is treated implicitly.

At far-field boundaries, the flux is computed using flow quantities from the adjacent cells and the freestream values determined as suggested by Srinivasan et al.[23] In this method, one-dimensional momentum theory is used to approximate the inflow/outflow boundary conditions by introducing a three-dimensional point sink concept to satisfy the conservation of mass. This boundary condition is a function of the rotor thrust coefficient, which is updated at every iteration as the calculation proceeds.

Because of the periodic nature of the flow for hovering rotors, calculations are performed for a single blade of the rotor, and the periodic boundary condition is applied between the blades. The grid periodicity is enforced at the grid-generation process, and the cells adjacent to this boundary are treated as interior cells so that no interpolation of flow is required.

Parallel Implementation

The numerical method described earlier is parallelized by partitioning the computational domain into several subdomains. Communication of the data between each processor is achieved using the message passing interface library. For the present cell-centered scheme, the data communication involves flow variables at the nodes, at the face centers, and at the adjacent cell centers of the domain boundaries. The partitioning is performed using the MeTiS[24] library considering the number of cells for each processor to achieve the load balancing. The code has been ported to a networked personal computer cluster system with Pentium III 500-MHz CPU processors. Calculations in the present paper are performed using eight nodes of the cluster system.

Solution-Adaptive Mesh Refinement

In the present study, the solution-adaptive mesh refinement is applied not only to capture high gradient flow regions on the blade but also to better resolve the tip vortex in the wake. The mesh adaptation indicator used for shock capturing is

$$\varepsilon_s = |\nabla^2 \rho| V_i \tag{7}$$

where the volume of each cell, V_i, is multiplied to prevent indefinite cell refinement.

Because the calculation is initiated on a relatively coarse mesh, the tip vortex shows a very rapid numerical dissipation, and the definite structure of the vortex core can be identified only in the near wake region from the tip of the blade. To capture the tip vortex extensively in the far wake and to preserve its strength, local mesh refinement needs to be performed through several adaptation levels along the tip vortex core location. The mesh coarsening is not performed.

At first, the location of local maximum of the vorticity[25] is searched for every 5 deg of vortex age starting from the trailing edge of the blade tip on two-dimensional cutting planes to locate the vortex core location. The search continues until the identification of the vortex core fails due to the numerical dissipation for a given mesh resolution. Next, the discrete vortex core locations are connected to form a smooth curve using a three-dimensional parabolic blending. Then, the cells on and near the captured tip vortex core trajectory located within six times of the local cell characteristic length are targeted for subdivision. The 1:8 division is made for the targeted cells by inserting a new grid point at the midpoint of each line of the six sides. Buffer cells are required between the targeted cells and the surrounding cells to confirm a valid cell connectivity. These buffer

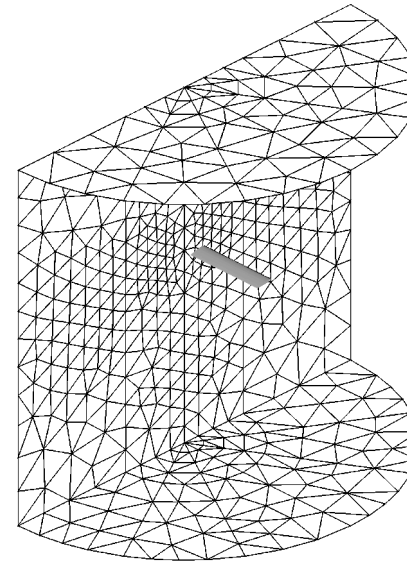

Fig. 1 Surface triangulation at the computational boundaries.

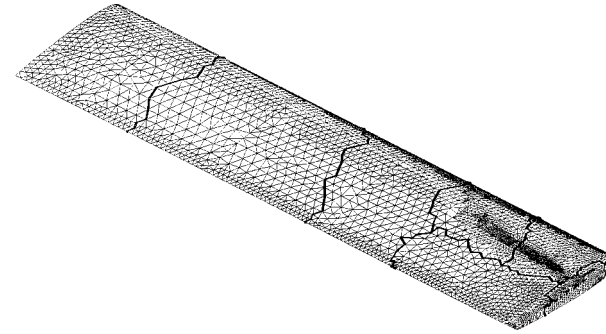

Fig. 2 Blade surface triangulation and parallel partitioning after two levels of adaptation at $M_T = 0.877$.

cells are divided as either 1:4 or 1:2. Because the targeted cells for 1:8 division are searched within six times of the local cell characteristic length from the center of the tip vortex core, the buffer cells are generally not divided subsequently as the cell size decreases. On the solid surface, the coordinates of inserted grid points are determined using a general three-dimensional surface curve fitting based on the Hermite polynomial interpolation to guarantee the smoothness.

The flow variables are interpolated on the added cell centers, and the calculation is resumed on the refined mesh. The refined mesh is repartitioned for load balancing after each mesh adaptation. The procedure is repeated until a satisfactory result is obtained for the blade loading and the tip vortex.

Computational Details

Calculations are made for a hovering rotor at two tip Mach numbers of 0.439 and 0.877, and the results are compared with Caradonna and Tung's experimental data.[17] The experimental model has a two-bladed, untwisted, rigid rotor. The blades are made of a

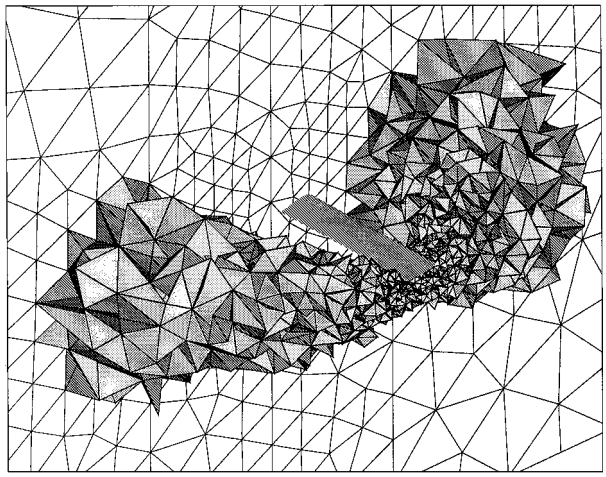

a) First-level adaptation (248,525 cells, 46,709 nodes)

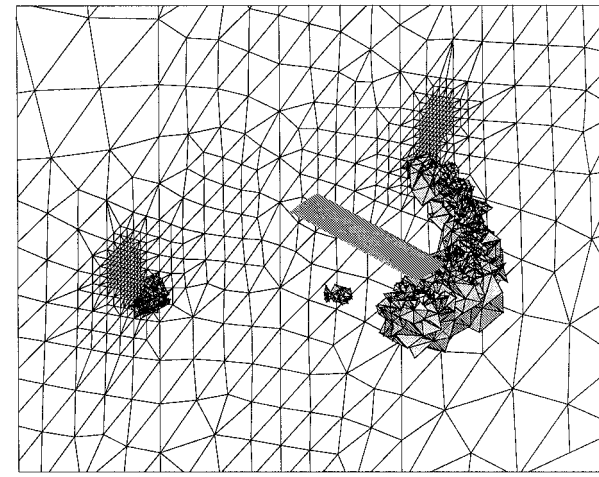

d) Fourth-level adaptation (414,644 cells, 75,280 nodes)

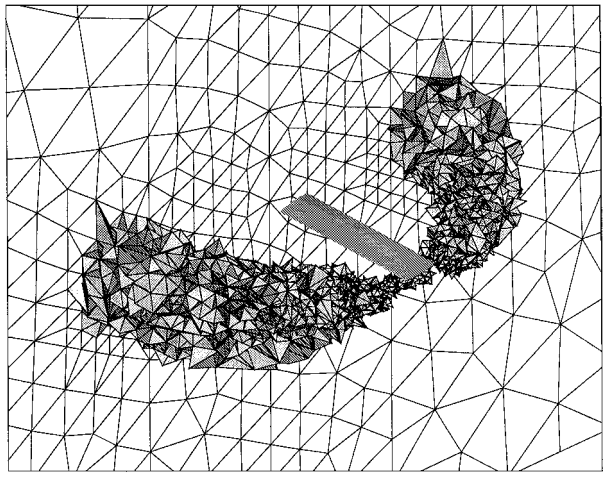

b) Second-level adaptation (311,229 cells, 57,457 nodes)

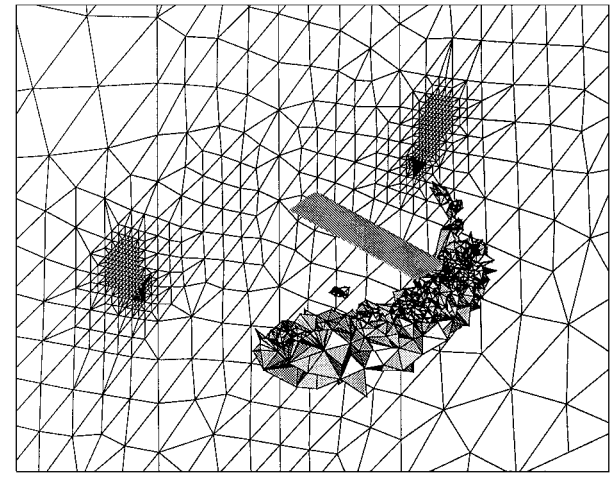

e) Fifth-level adaptation (429,960 cells, 77,923 nodes)

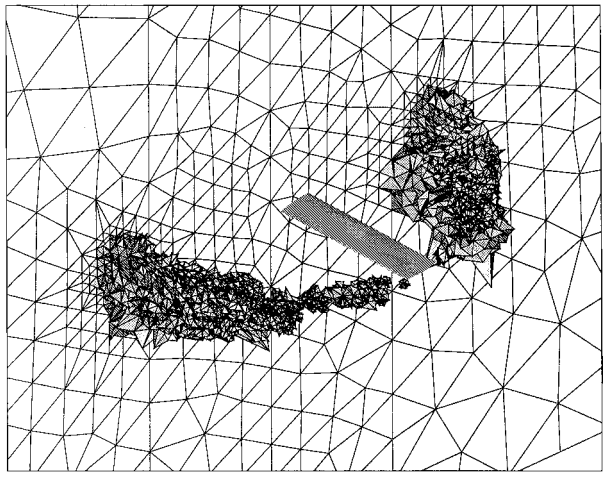

c) Third-level adaptation (397,301 cells, 72,254 nodes)

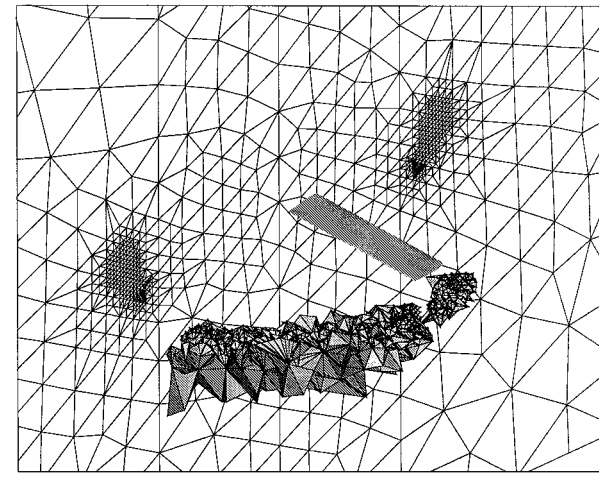

f) Sixth-level adaptation (444,723 cells, 80,488 nodes)

Fig. 3 Mesh adaptation sequence for the wake at $M_T = 0.439$.

NACA 0012 airfoil section with a rectangular planform of an aspect ratio equal to 6. Both cases computed for the present paper have a collective pitch angle of 8 deg. The unstructured tetrahedral meshes used for the present calculations are generated by using an advancing-front technique.[26]

The initial three-dimensional mesh consists of 201,719 tetrahedra and 37,770 node points, which is considered to be very coarse compared to that of other researchers.[14,16] The surface triangulation on the blade contains 12,414 triangles and 6,209 node points. The far-field boundaries are located at two radii downstream of the rotor, one and one-half radii upstream of the rotor, and two radii away from the center of rotation in the radial direction, which are similar to those used by previous researchers.[9,11,13,14,16] Figure 1 shows the computational domain with the surface triangles at the computational boundaries. The grid periodicity is confirmed at the periodic boundaries between the blades in Fig. 1.

At first, calculations are made on the same initial mesh for both subsonic and transonic cases. Then, surface adaptations are made based on the initial mesh solution to improve the solution accuracy on the blade. For the subsonic case, one-level mesh adaptation is made for the high flow gradients at the leading edge and near the tip. An additional level of surface adaptation is made for the transonic tip Mach number case for a better shock resolution. After each of the mesh adaptation procedures, new domain partitioning is obtained to achieve the load balancing for parallel computing. After the surface adaptations, the mesh size increased to 221,772 tetrahedra and 42,074 nodes for the subsonic case and 242,631 tetrahedra and 46,543 nodes for the transonic. Figure 2 shows the blade surface mesh after two levels of surface adaptation at transonic speed confirming high grid density along the shock formation. Figure 2 also shows the partitioned subdomain boundaries for parallel computing.

In the rotor wake region, six levels of mesh adaptation are made at the subsonic tip Mach number and five levels for the transonic case. The cells targeted along the tip vortex core location are divided until the characteristic length scale of each cell becomes less than

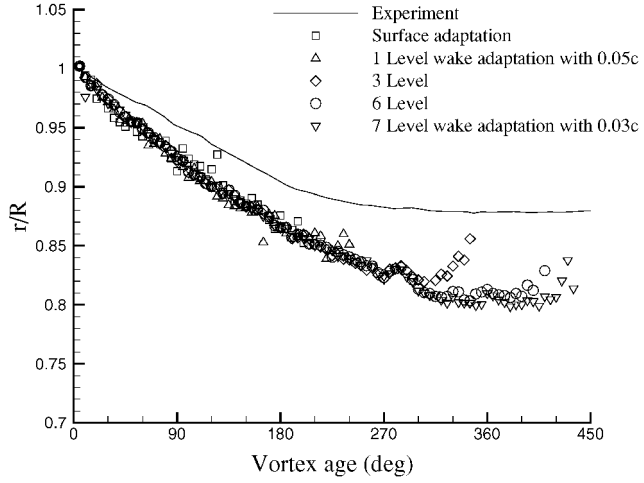

a) Tip vortex contraction

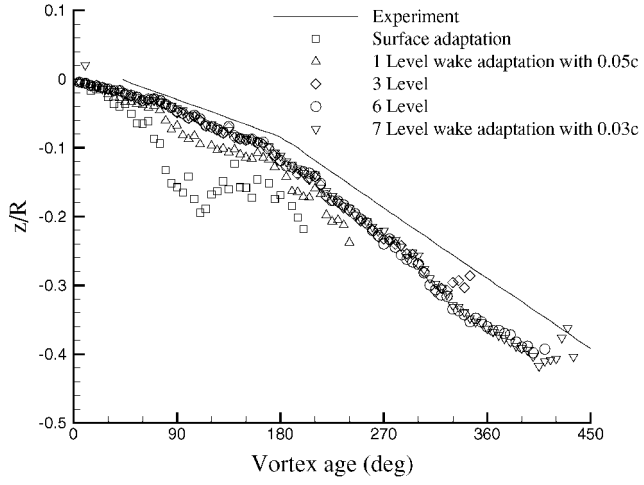

b) Tip vortex descent

Fig. 4 Effect of mesh adaptation on predicted tip vortex geometry at $M_T = 0.439$.

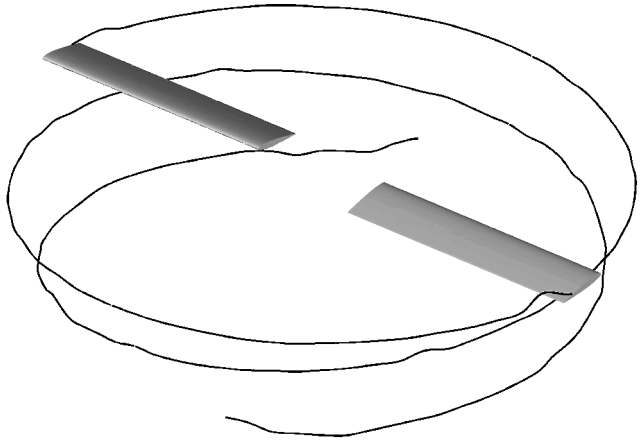

Fig. 5 Computed tip vortex core trajectory at $M_T = 0.439$.

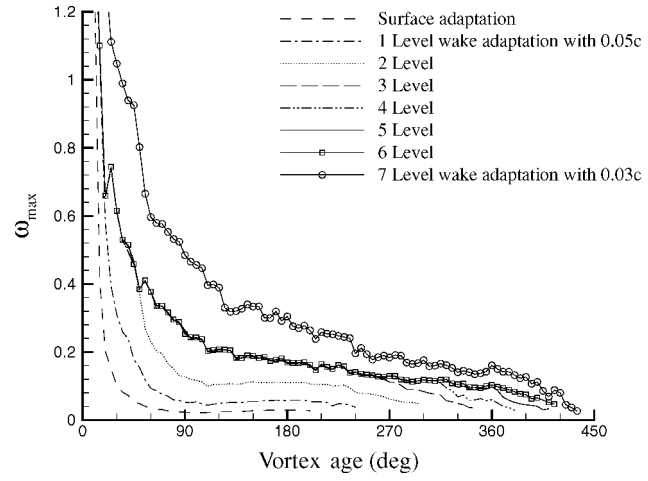

Fig. 6 Maximum vorticity of the tip vortex core along the vortex age at $M_T = 0.439$.

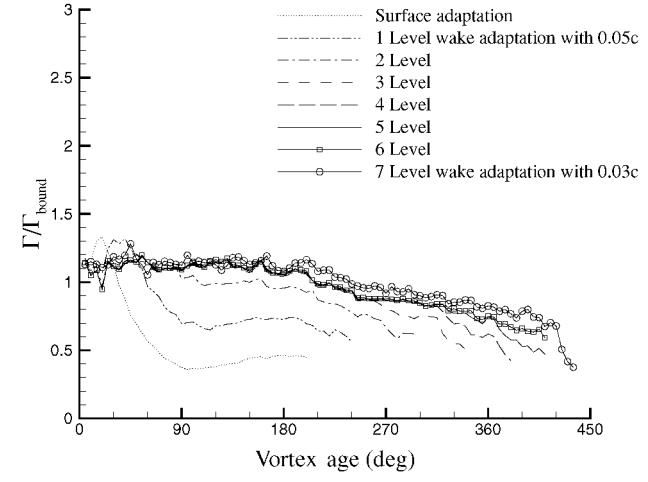

Fig. 7 Effect of mesh adaptation on tip vortex strength along the vortex age at $M_T = 0.439$.

0.05 fraction of the blade chord length. The cell size criterion of the mesh adaptation is so chosen because it is equivalent to the size of the finest wake grid used by Ahmad and Strawn.[13] In addition to the cells along the currently detected tip vortex trajectory, an additional 20 deg of vortex age are also adapted at each adaptation level downstream of the last detected tip vortex core location to prevent numerical dissipation and to help the vorticity transportation mechanism. The additional adaptation is performed for cells on and around a three-dimensional curve obtained by extrapolating the current tip vortex trajectory. The final mesh consists of 444,723 tetrahedra and 80,488 nodes for the subsonic case. The final mesh for the transonic case contains 454,028 tetrahedra and 83,008 nodes. One additional level of wake adaptation is added for the subsonic case by refining the cells along the tip vortex to obtain a targeted cell size less than 0.03 chord length to test the grid size dependency. The additional adaptation leads to 617,997 tetrahedra and 110,396 nodes.

The flow solver runs at an approximate speed of 160 μs CPU time per cell per iteration per processor on the personal computer cluster. The total elapsed computational time required for the converged solution on the finest mesh is about 11 h using eight processors.

Results and Discussion

Figure 3 shows the wake adaptation sequence for the subsonic tip Mach number case. In Fig. 3, targeted cells for subdivision are shown at several adaptation levels, which represent the relative size of the mesh at the particular adaptation level. The surface triangulation on the periodic boundaries is also shown in Fig. 3. It is shown that the initial mesh has a very large characteristic cell size relative to the blade chord length away from the blade, which is not appropriate at all for preserving the tip vortex. As adaptations proceed and the tip vortex establishes, the relative size of the cells decreases. After several levels of adaptation, the cells near the tip vortex become

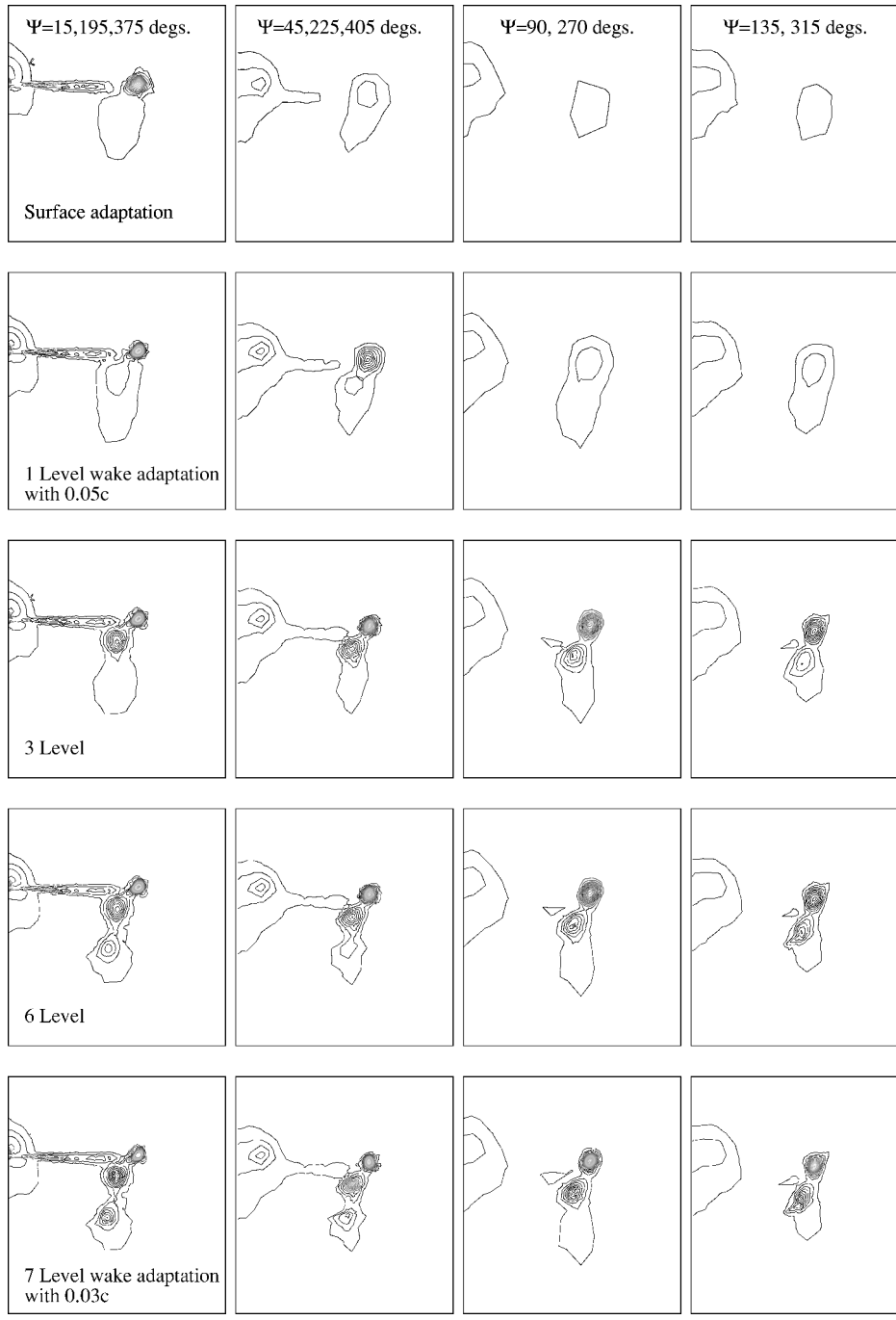

Fig. 8 Vorticity contours at various vortex ages at $M_T = 0.439$ (minimum = 0.02, maximum = 1.00, and interval = 0.02).

smaller than the targeted cell size of 0.05 chord length so that no cells are allowed for subdivision as shown at the fourth level in the near wake. At the same time, the wake adaptation is pushed farther downstream of the wake while the tip vortex exposes itself for a wider range of vortex age as the numerical dissipation decreases. The surface triangulation on the periodic boundaries clearly represents the effect of adaptation showing the approximate locations of the primary tip vortex core from the current blade tip and the one from the preceding blade.

The corresponding tip vortex geometries at each level of wake adaptation from Fig. 3 are shown and compared with the experimental data in Fig. 4. When the initial coarse mesh after the surface adaptation is used, it is shown that the tip vortex can be identified only up to 200 deg of the vortex age. Also, the vertical descent of the tip vortex is predicted to be more rapid than the experiment. As the wake adaptation proceeds and the numerical dissipation is reduced, the tip vortex core is identified farther downstream, and the predicted geometry of the core approaches the experiment.

Finally, after the sixth level of adaptation, the tip vortex is captured up to 410 deg of vortex age. The result compares well with the experiment within the accuracy of other numerical predictions.[13,14] An additional adaptation with 0.03 chord length mesh size does not significantly alter the converged tip vortex trajectory obtained after the sixth-level adaptation. The perspective view of the predicted tip vortex trajectory from the two blades is shown in Fig. 5 for the vortex age of approximately 410 deg. A very similar tip vortex trajectory behavior is also obtained for the transonic tip Mach number case and is not included in the paper.

In Fig. 6, the effect of wake mesh adaptation on the strength of the tip vortex core is presented. In Fig. 6, the maximum vorticity value inside the tip vortex core is shown for the vortex age at different levels of wake adaptation. The vorticity distribution along the tip vortex trajectory obtained on the initial coarse mesh shows a very rapid drop of the value due to the excessive numerical dissipation. As the level of wake adaptation increases, the vorticity preserves its strength better as expected on finer meshes. An additional wake adaptation with 0.03 chord length scale predicts higher vorticity level than that of the final result with 0.05c. Thus, the use of 0.03 chord length scale for the wake mesh adaptation may not guarantee the grid convergence as far as the maximum vorticity strength is concerned.

The overall strength of the tip vortex along the vortex age is shown in Fig. 7 for different levels of wake adaptation. The tip vortex strength is calculated by integrating the distributed vorticity over the vortex core at each section of the tip vortex. The approximate boundary of the tip vortex core is identified to have the vorticity strength higher than 10% of that of the maximum value at the center of the core. The calculated tip vortex strength is normalized by the maximum bound circulation of the blade obtained from the converged

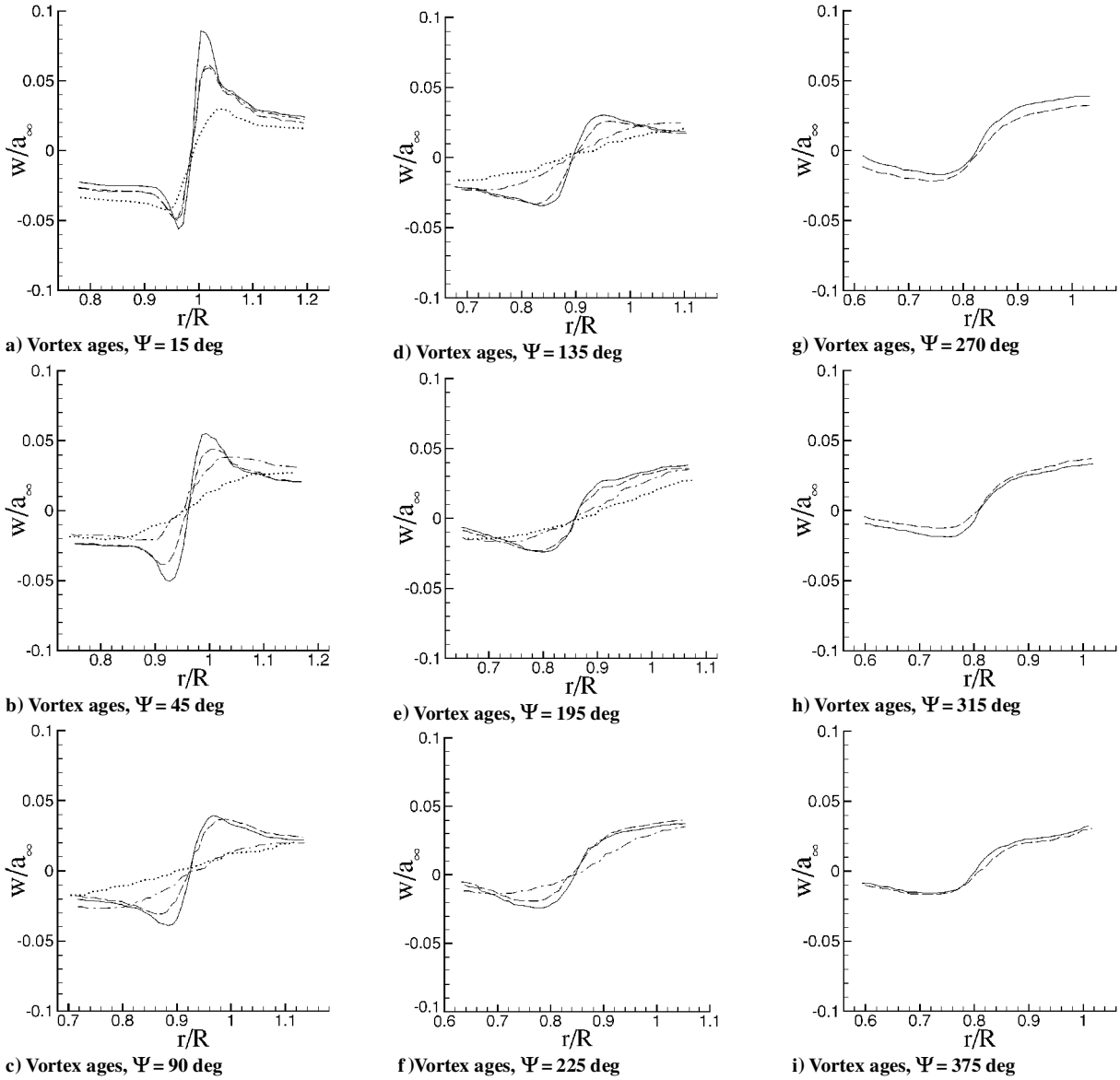

Fig. 9 Induced velocity profiles at various vortex ages at $M_T = 0.439$: where · · · · is initial mesh; — · — first-level wake adaptation with 0.05c; – – – sixth-level adaptation, and —— seventh-level wake adaptation with 0.03c.

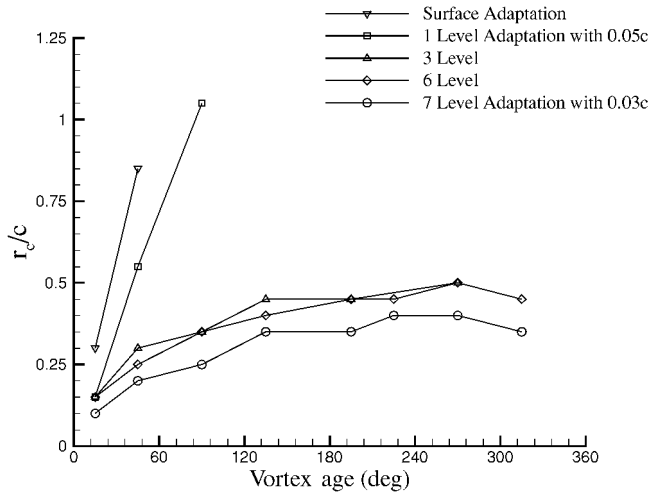

Fig. 10 Growth of the tip vortex core along the vortex age at $M_T = 0.439$.

solution after each level of mesh adaptation. For the few early mesh adaptation stages, a very rapid dissipation of the tip vortex strength is observed, as in the case of the maximum vorticity level in Fig. 6. As the adaptation proceeds, the strength of the tip vortex converges along the vortex age. It is found that the wake adaptation with 0.05 chord length scale for the present second-order spatially accurate scheme preserves the tip vortex strength up to approximately 70% of its original bound vortex on the blade at least for 420 deg of vortex age. An additional wake adaptation with 0.03 chord length scale improves the result by approximately 10% especially after 180 deg of vortex age.

The predicted vorticity contours at various locations in the rotor wake for the subsonic tip Mach number case are presented in Fig. 8. The azimuthal position of these cutting planes are 15, 45, 90, and 135 deg behind the blade. It is found that the tip vortex predicted on the initial mesh is very diffusive, and only the primary tip vortex from the current blade is reasonably well captured at 15 deg of the vortex age. The inboard vortex sheet is also captured well at this azimuthal location. It is shown that as the wake adaptation proceeds providing finer meshes the tip vortex core becomes clearer not only in the wake behind the blade but also in the region ahead of the

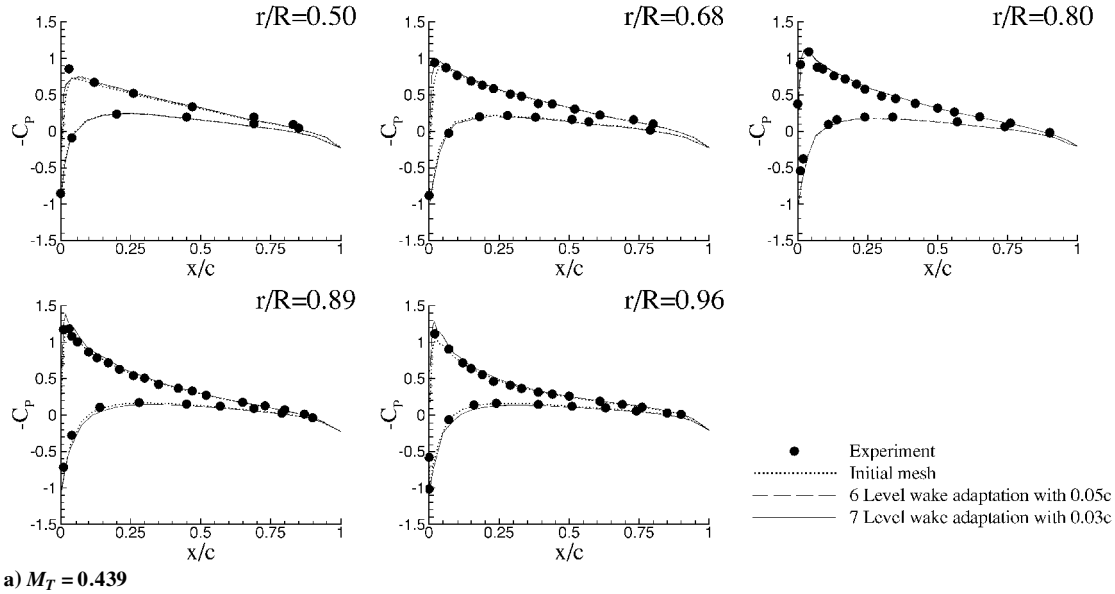

a) $M_T = 0.439$

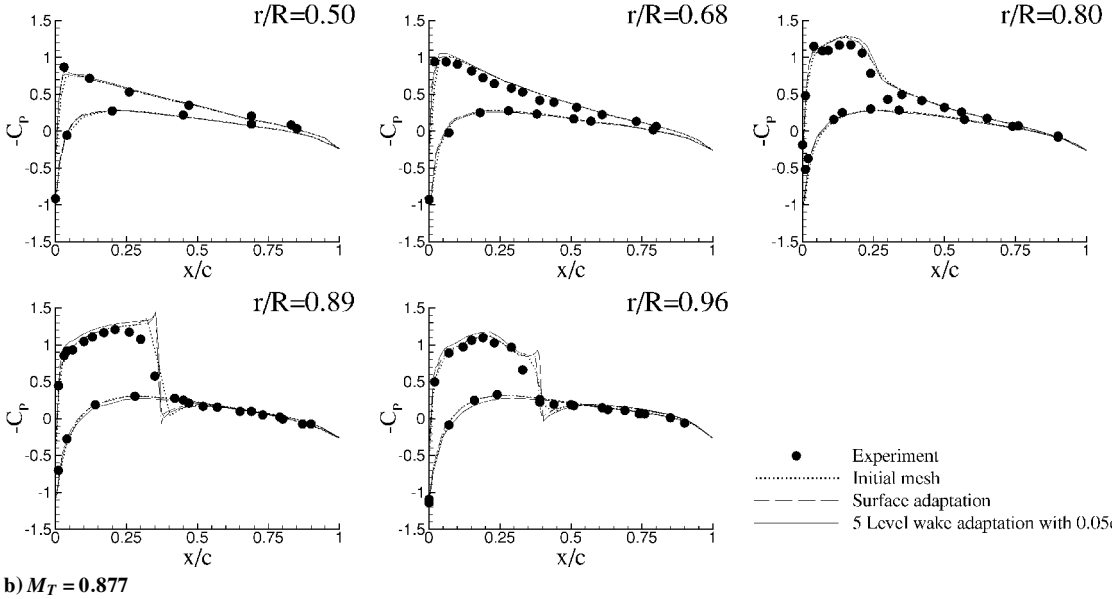

b) $M_T = 0.877$

Fig. 11 Pressure coefficient distributions on the blade.

current blade location simulating the tip vortex originating from the preceding blade. This implies that the flow periodicity imposed by the present solver successfully transports the vorticity through the periodic boundaries. The numerical formation of the tip vortex from the preceding blade becomes much clearer after the third level of wake adaptation. After the sixth level of adaptation, the third layer of the tip vortex from the current blade after more than one revolution is clearly captured. An additional wake adaptation with 0.03 chord length scale seems to improve the vortex resolution at all wake locations. The inboard root vortex is also shown even though no attempt of mesh adaptation is made.

Figure 9 shows the vertical induced velocity profile at the same vortex ages shown in Fig. 8. As the mesh adaptation proceeds, the captured tip vortex structure better resolves its peak-to-peak vertical velocity at all vortex ages, as expected from Fig. 6 and 8. The peak of the induced velocity profile quickly disappears within the near wake of 45 deg of vortex age without wake mesh adaptations. After the seventh level of wake adaptation, the peak inside the wake boundary is clearly identified up to 315 deg of vortex age representing reduced numerical diffusion for resolving the tip vortex. It is also shown that the peak of vertical induced velocity at the outer region of the core disappears after 180 deg of vortex age due to the mutual interaction between the current tip vortex and the one above from the preceding blade. The size of the tip vortex core is estimated from the vertical induced velocity profile and presented in Fig. 10. It is demonstrated that the predicted tip vortex core size is significantly reduced from approximately 1.05 chord length before the wake adaptation to 0.25 after the the seventh level of wake adaptation at 90 deg of vortex age. Although the predicted tip vortex core diameter is slightly bigger than typical values of 10–15% of the blade chord length, the qualitative behavior is consistent with experimental results[27,28] showing a rapid initial growth followed by a logarithmic trend in its size.

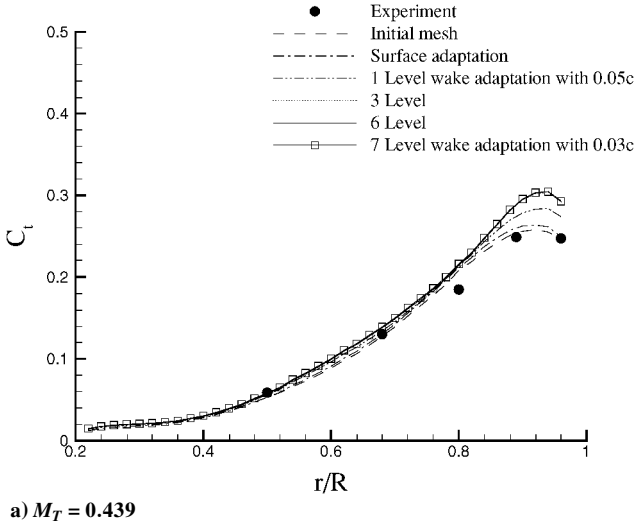

a) $M_T = 0.439$

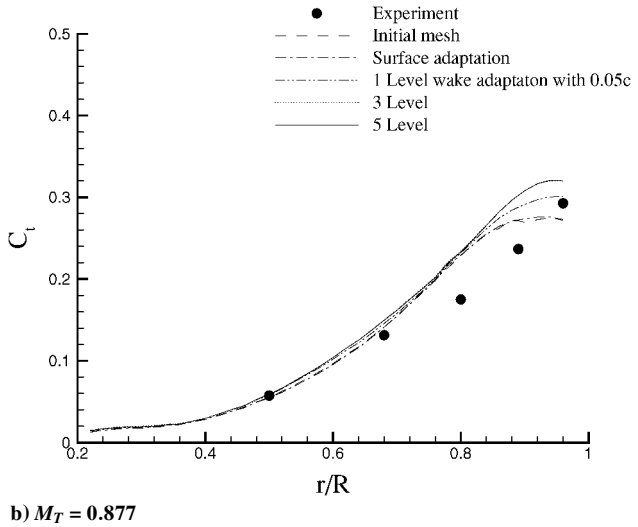

b) $M_T = 0.877$

Fig. 12 Spanwise sectional thrust coefficient distributions.

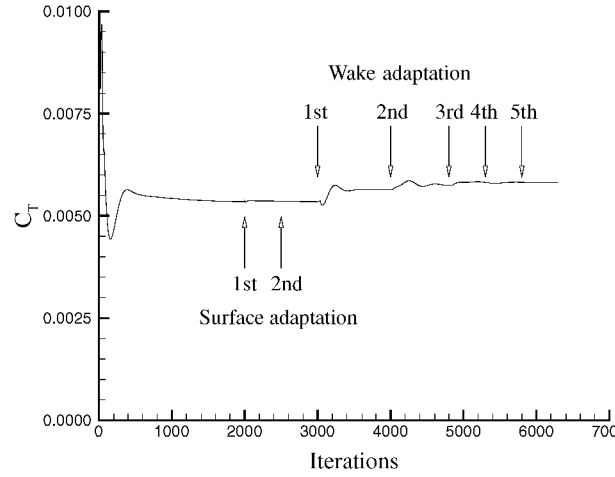

Fig. 13 Convergence history of the rotor thrust coefficient at $M_T = 0.877$.

Figure 11 shows the surface pressure coefficient distributions at several radial locations of the blade for both subsonic and transonic tip Mach numbers. The converged results from the mesh adaptation show good agreement with the experimental data. Slightly better results are shown near the leading edge of the blade due to the improved mesh resolution, particularly for the subsonic case. A sharper shock definition is also obtained after a couple of surface mesh refinements for the transonic tip Mach number operating condition. It is also shown that the wake mesh adaptation changes the predicted value of pressure particularly on the lower surface of the blade at spanwise locations near the blade tip. This is due to the interaction between the blade and the tip vortex from the preceding blade, which passes under the current blade at approximately 85% spanwise location with an enhanced vortex strength resulting from the wake mesh refinement.

Figure 12 shows the sectional thrust distributions along the blade span at the two tip Mach numbers. The predicted values are slightly higher than the experiment especially toward the tip of the blade, which is consistent with the results obtained by previous researchers.[13,14] The strong tip vortex formation under the blade with refined meshes induces an upwash causing an effect of increasing the local effective angles of attack at the outboard of the tip vortex location originating from the preceding blade. The vortex age of 180 deg is the location where the tip vortex has the most influence on the blade airloads. The effect of additional wake adaptation with 0.03 chord length scale is not very significant as far as the sectional loading is concerned.

Finally, the convergence history of total rotor thrust coefficient is presented for the transonic tip Mach number in Fig. 13. The first few levels of wake adaptation increase the total thrust as the tip vortex formation gets stronger as described earlier for the sectional loading distributions. The predicted total thrust is slightly higher than that of the experiment mainly due to the lack of viscous mechanism of the present inviscid flow solver.

Conclusions

A three-dimensional inviscid flow solver is developed for simulating the flowfield of hovering helicopter rotor using a solution-adaptive unstructured mesh refinement technique. It is demonstrated that an accurate prediction of both the blade loading and the tip vortex trajectory can be achieved through a series of surface and wake mesh adaptations with the final mesh size less than 500,000 cells. The local wake mesh refinement procedure enables capturing the tip vortex up to 420 deg of the vortex

age by reducing numerical dissipation. The cell subdivision using a 0.05 chord length adaptation scale seems to be sufficient for the accurate prediction of blade loading and the tip vortex preservation using the present second-order spatially accurate numerical method. An additional refinement test with a 0.03 chord length scale is also performed for a grid size dependency test. Calculations are performed for two experimental rotor operating conditions. The results show good agreement with experimental data for both the blade loading and the tip vortex behavior.

References

[1]Johnson, W., "Development of a Comprehensive Analysis for Rotorcraft I. Rotor Model and Wake Analysis," *Vertica*, Vol. 5, 1981, pp. 99–130.

[2]Egolf, T. A., and Sparks, S. P., "A Full Potential Flow Analysis with Realistic Wake Influence for Helicopter Rotor Airload Prediction," NASA CR 4007, Jan. 1987.

[3]Agarwal, R. K., and Deese, J. E., "Euler Calculations for a Flowfield of a Helicopter Rotor in Hover," *Journal of Aircraft*, Vol. 24, No. 4, 1987, pp. 231–238.

[4]Srinivasan, G. R., and McCroskey, W. J., "Navier–Stokes Calculations of Hovering Rotor Flowfields," *Journal of Aircraft*, Vol. 25, No. 10, 1988, pp. 865–874.

[5]Wake, B. E., and Sankar, N. L., "Solutions of the Navier–Stokes Equations for the Flow About a Rotor Blade," *Journal of the American Helicopter Society*, Vol. 34, No. 2, 1989, pp. 13–23.

[6]Ramachandran, K. C. T., and Caradonna, F. X., "Rotor Hover Performance Prediction Using a Free-Wake, Computational Fluid Dynamics Method," *Journal of Aircraft*, Vol. 26, No. 12, 1989, pp. 1105–1110.

[7]Chen, C. L., and McCroskey, W. J., "Numerical Simulation of Helicopter Multi-Bladed Rotor Flow," AIAA Paper 88–0046, Jan. 1988.

[8]Srinivasan, G. R., Baeder, J. D., Obayashi, S., and McCroskey, W. J., "Flowfield of a Lifting Rotor in Hover: A Navier–Stokes Simulation," *AIAA Journal*, Vol. 30, No. 10, 1992, pp. 2371–2378.

[9]Wake, B. E., and Baeder, J. D., "Evaluation of a Navier–Stokes Analysis Method for Hover Performance Prediction," *Journal of the American Helicopter Society*, Vol. 41, No. 1, 1996, pp. 7–17.

[10]Duque, E. P. N., and Srinivasan, G. R., "Numerical Simulation of a Hovering Rotor using Embedded Grids," *Proceeding of the 48th Annual Forum of the American Helicopter Society*, American Helicopter Society, Alexandria, VA, 1992, pp. 429–445.

[11]Hariharan, N. S., and Sankar, L. N., "First-Principles Based High Order Methodologies for Rotorcraft Flowfield Studies," *Proceedings of 55th Annual Forum of the American Helicopter Society*, American Helicopter Society, Alexandria, VA, 1999, pp. 1921–1933.

[12]Tang, L., and Baeder, J. D., "Improved Euler Simulation of Hovering Rotor Tip Vortices with Validation, *Proceedings of 55th Annual Forum of the American Helicopter Society*, American Helicopter Society, Alexandria, VA, 1999, pp. 1934–1948.

[13]Ahmad, J. U., and Strawn, R. C., "Hovering Rotor and Wake Calculations with an Overset-Grid Navier–Stokes Solver," *Proceedings of 55th Annual Forum of the American Helicopter Society*, American Helicopter Society, Alexandria, VA, 1999, pp. 1949–1959.

[14]Strawn, R. C., and Barth, T. J., "A Finite-Volume Euler Solver for Computing Rotary-Wing Aerodynamics on Unstructured Meshes," *Journal of the American Helicopter Society*, Vol. 38, No. 2, 1993, pp. 61–67.

[15]Duque, E. P. N., Biswas, R., and Strawn, R. C., "A Solution Adaptive Structured/Unstructured Overset Grid Flow Solver with Applications to Helicopter Rotor Flows," AIAA Paper 95–1766, June 1995.

[16]Dindar, M., Lemnios, A., Shephard, M., Jansen, K., and Kenwright, D., "Effect of Tip Vortex Resolution on UH-60A Rotor-Blade Hover Performance Calculations," *Proceeding of the 54th Annual Forum of the American Helicopter Society*, American Helicopter Society, Alexandria, VA, 1998, pp. 45–57.

[17]Caradonna, F. X., and Tung, C., "Experimental and Analytical Studies of a Model Helicopter Rotor in Hover," NASA TM 81232, Sept. 1981.

[18]Roe, P. L., "Approximate Riemann Solvers, Parameter Vectors and Difference Schemes," *Journal of Computational Physics*, Vol. 43, No. 2, 1981, pp. 357–372.

[19]Chen, C. L., McCroskey, W. J., and Obayashi, S., "Numerical Solutions of Forward-Flight Rotor Flow Using an Upwind Method," *Journal of Aircraft*, Vol. 28, No. 6, 1991, pp. 374–380.

[20]Frink, N. T., "Upwind Scheme for Solving the Euler Equations on Unstructured Tetrahedral Meshes," *AIAA Journal*, Vol. 30, No. 1, 1992, pp. 70–77.

[21]Holmes, D. G., and Connell, S. D., "Solution of the Two-Dimensional Navier–Stokes Equations on Unstructured Adaptive Grids," AIAA Paper 89-1932, June 1989.

[22]Anderson, W. K., "Grid Generation and Flow Solution Method for Euler Equations on Unstructured Grid," NASA TM 4295, April 1992.

[23]Srinivasan, G. R., and Raghavan, V., and Duque, E. P. N., "Flowfield Analysis of Modern Helicopter Rotors in Hover by Navier–Stokes Method," *Journal of the American Helicopter Society*, Vol. 38, No. 3, 1993, pp. 3–13.

[24]Karypis, G., and Kumar, V., "Multilevel k-Way Partitioning Scheme for Irregular Graphs," *Journal of Parallel and Distributed Computing*, Vol. 48, No. 1, 1998, pp. 96–129.

[25]Strawn, R. C., Kenwright, D. N., and Ahmad, J., "Computer Visualization of Vortex Wake Systems," *AIAA Journal*, Vol. 37, No. 4, 1999, pp. 511, 512.

[26]Löhner, R., and Parikh, P., "Generation of Three-Dimensional Unstructured Grids by the Advancing Front Method," *International Journal of Numerical Methods in Fluids*, Vol. 8, 1988, pp. 1135–1149.

[27]Thomson, T. L., Komerath, N. M., and Gray, R. B., "Visualization and Measurement of the Tip Vortex Core of a Rotor Blade in Hover," *Journal of Aircraft*, Vol. 25, No. 2, 1988, pp. 1113–1121.

[28]Leishman, J. G., Baker, A., and Coyne, A., "Measurements of Rotor Tip Vortices Using Three-Component Laser Doppler Velocimetry," *Journal of the American Helicopter Society*, Vol. 41, No. 4, 1996, pp. 342–253.